Transition to the ultimate regime of turbulent convection in stratified inclined duct flow

Rundong Zhou [1], Adrien Lefauve [2,3], Roberto Verzicco [1,4,5] and Detlef Lohse [1,6]

[1] *Physics of Fluids Department, J.M. Burgers Center for Fluid Dynamics and Max Planck Center Twente for Complex Fluid Dynamics, Faculty of Science and Technology, University of Twente, P.O. Box 217, 7500 AE Enschede, Netherlands*

[2] *Grantham Institute—Climate Change and the Environment, Imperial College, London SW7 2AZ, United Kingdom*

[3] *Department of Civil and Environmental Engineering, Imperial College, London SW7 2BU, United Kingdom*

[4] *Dipartimento di Ingegneria Industriale, University of Rome "Tor Vergata," 00133 Rome, Italy*

[5] *Gran Sasso Science Institute, Viale F. Crispi 7, 67100 L'Aquila, Italy*

[6] *Max Planck Institute for Dynamics and Self-Organization, Am Fassberg 17, 37077 Göttingen, Germany*

(Received 15 August 2025; revised 5 December 2025; accepted 2 March 2026; published 7 April 2026)

The stratified inclined duct (SID) provides a canonical setup for sustained, buoyancy-driven exchange flow between two reservoirs of different density, and emerges as a paradigm in geophysical fluid dynamics. Yet, the flow dynamics remain unclear in the highly turbulent regime; laboratory experiments can access this regime but they lack resolution, while direct numerical simulations (DNSs) at realistically high Prandtl number, $\mathrm{Pr} = 7$ (for heat in water), have not achieved sufficiently high Reynolds numbers Re. We conduct three-dimensional DNSs up to $\mathrm{Re} = 8000$ and observe the transition to the so-called ultimate regime of turbulent convection as evidenced by the Nusselt number scaling $\mathrm{Nu} \sim \mathrm{Ra}^{1/2}$, indicating substantially enhanced transport. At the transition, the shear Reynolds number, a key parameter characterizing boundary layer (BL) dynamics, exceeds the threshold range of 420 for turbulent kinetic BLs with the emergence of logarithmic velocity profiles. The nature of the transition toward ultimate SID flow is non-normal-nonlinear, i.e., subcritical and hysteretic, as is typical for the transition to fully turbulent shear flows. Our work connects SID flow with the broader class of wall-bounded turbulent convection flows and gives insight into mixing properties in the vigorously turbulent regime encountered in oceanographic and industrial flows.

DOI: 10.1103/psz6-f48t

I. INTRODUCTION

Buoyancy-driven exchange flows occur in many natural and built environments when two large bodies of fluid at different densities are connected through a narrow channel. Such flows cause significant exchange of scalars (e.g., heat, salt, pollutants, and nutrients) between the two reservoirs with minimal to no net volume transport [1,2]. They underpin key mixing and transport processes in oceanography and industrial flows. For example, the Mediterranean Sea depends on exchanges through the Strait of Gibraltar and the Bosphorus [3], coastal environments depend on estuarine

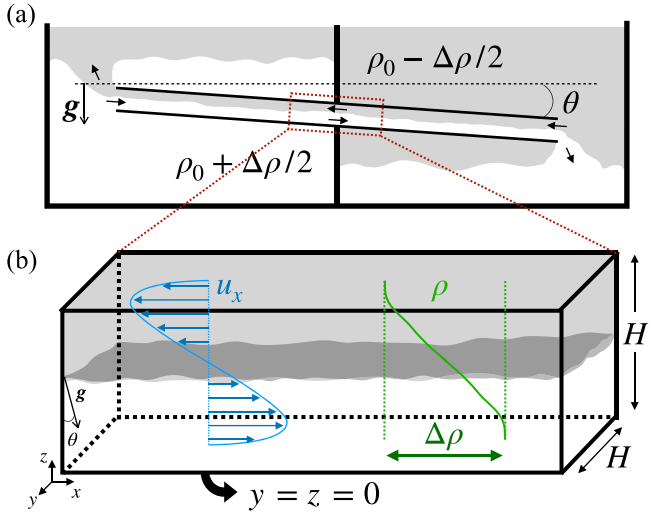

FIG. 1. (a) Schematic illustration of the SID experiment. (b) Detail of the mid-duct region in the duct reference frame, showing typical vertical profiles of mean streamwise velocity (blue) and density (green).

transport processes [4,5], and natural air ventilation in buildings and industrial safety scenarios depend on exchange between stratified air masses [6]. Moreover, these flows are inherently stably stratified shear flows, ideal for studying shear instabilities and sustained stratified turbulence, a research lineage extending back to seminal works by Reynolds [7] and Taylor [8].

The stratified inclined duct (SID) experiment was developed to study such buoyancy-driven exchange flows with sustained shear under well-controlled conditions [9], serving as a continuous realization of Thorpe's seminal closed tilted-channel experiments [10]. The SID is schematically illustrated in Fig. 1: Two reservoirs are filled with liquids of different densities $\rho_0 \pm \Delta\rho/2$, connected via a long rectangular duct tilted at an angle θ from the horizontal in the laboratory frame. Once the duct is opened, a transient gravity current occurs, after which a sustained, buoyancy-driven, two-layer stratified exchange flow develops. SID flow has emerged as a paradigm in fluid mechanics for exploring the routes to stratified turbulence, exhibiting rich transitional and intermittent dynamics which have been well documented over the past decade [9,11–17] (for a review, see Ref. [18]). With increased driving, either through larger density differences $\Delta\rho/\rho_0$ or greater inclination θ, the flow typically transitions through four qualitatively distinct regimes: laminar, wave, intermittently turbulent, and fully turbulent.

The dimensionless Rayleigh number,

$$\mathrm{Ra} \equiv \frac{g(\Delta\rho/\rho_0)H^3}{\nu\kappa}, \tag{1}$$

quantifies the strength of the buoyancy driving, where H is the duct height and serves as the characteristic length scale, ν is the kinematic viscosity, κ is the thermal diffusivity, and g is the gravitational acceleration. Ra serves as a primary control parameter along with the inclination θ. The hydraulic Reynolds number, sometimes used in the literature,

$$\mathrm{Re} \equiv \frac{\sqrt{g(\Delta\rho/\rho_0)H}(H/2)}{\nu} = \frac{1}{2}\,\mathrm{Ra}^{1/2}\,\mathrm{Pr}^{-1/2}, \tag{2}$$

is an equivalent parameter to Ra in this work as we fix the Prandtl number, $\mathrm{Pr} \equiv \nu/\kappa = 7$, approximating heat in water around 20°C. For salt in water, the corresponding $\mathrm{Pr}_s \equiv \nu/D = 700$ (also called Schmidt number, Sc), with D being the molecular diffusivity, is two orders of magnitude larger. The velocity scale is the free-fall velocity $U_0 \equiv \sqrt{g(\Delta\rho/\rho_0)H}$, the typical observed peak

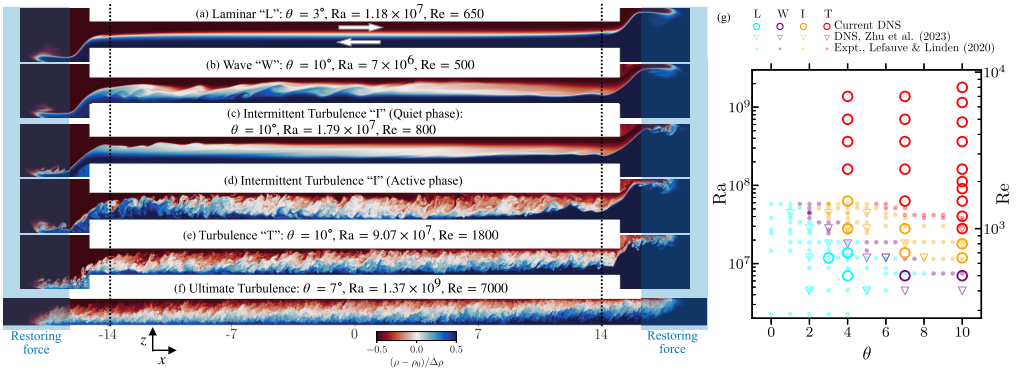

FIG. 2. [(a)–(f)] Snapshots of the spanwise midplane density field ρ for increasingly turbulent flow regimes. The flow directions are indicated by arrows in (a). The z axis is scaled up by 1.5. Simulations include artificial restoring forces applied in the blue regions (see the Appendix). The quantities are averaged within $x/H \in [-14, 14]$ (dashed black lines) to eliminate edge effects. (g) Qualitative flow regime phase diagram illustrating the current direct numerical simulation (DNS) results alongside previous experimental [12] and numerical [15] data at $\mathrm{Pr} = 7$.

velocity, while the length scale is $H/2$ in Re [18]. The regimes are visualized by the density field snapshots and classified by the phase diagram in Fig. 2.

A key feature of SID flow is that its shear is generated exclusively by buoyancy, distinguishing it from canonical sheared convective flows that are typically driven mechanically [19–21], or by external forcing mechanisms and imposed pressure gradients [22,23]. Additionally, it is bounded by no-slip sidewalls. These characteristics connect SID flow to other extensively studied canonical buoyancy-driven wall-bounded systems such as Rayleigh-Bénard (RB) convection (flow heated from below and cooled from above in an enclosed domain) [24–29], axially homogeneous RB convection, also known as convection in a vertical channel (CVC) [30–33], vertical convection (flow between two vertical heated and cooled plates) [34–38], and Taylor-Couette flow (flow between two coaxial co- or counterrotating cylinders) [39–41]. In particular, for an extreme $\theta = 90^\circ$, SID flow is a realization of CVC, where the heated and cooled plates of RB convection are replaced by reservoirs. For small θ, SID flow retains distinct features of a stably stratified, strongly sheared mean exchange flow. In spite of the recent interest, SID flow characteristics in the strongly turbulent regime have remained out of reach. Experiments have reached $\mathrm{Re} = O(10^4)$ at $\mathrm{Pr}_s = 700$ [12,16] but measurements of the velocity and density fields have so far been restricted to $\mathrm{Re} = O(10^3)$ [13,14]. Likewise, numerical simulations resolve the full flow fields but have also been restricted to $\mathrm{Re} = O(10^3)$ at $\mathrm{Pr} = 7$ [15].

In this work, we overcome these limitations by directly simulating highly turbulent SID flow up to $\mathrm{Re} = 8000$, corresponding to $\mathrm{Ra} = 1.8 \times 10^9$ [see Fig. 2(g)]. Our main finding is a pronounced enhancement in mass transfer efficiency beyond a threshold of $\mathrm{Ra} \approx 10^8$, with the scaling shifting from $\mathrm{Nu} \sim \mathrm{Ra}^{1/3}$ to $\mathrm{Nu} \sim \mathrm{Ra}^{1/2}$, consistent with the so-called ultimate regime of turbulent thermal convection first proposed by Kraichnan [42] and found in homogeneous RB convection [31]. This transition is concomitant with the development of turbulent boundary layers (BLs), suggesting an alternative turbulent channel configuration. These results provide an observation of the ultimate regime in SID flow, and three-dimensional (3D) numerical evidence of turbulent BLs in a purely buoyancy-driven system as previously found in vertical convection [38].

The paper is organized as follows. In Sec. II, we introduce the governing equations and the numerical schemes used to solve them. In Sec. III, we present the main results on global response parameters: Sec. III A demonstrates the transition to ultimate scaling in the mass flux; Sec. III B quantifies the energy budget and mixing, and discusses quantities of particular interest to the

oceanography and stratified turbulence communities; and Sec. III C explains the physical origin of the observed ultimate scaling. Section IV is on the local properties of the flow: We provide evidence for turbulent boundary layers in Secs. IV A and IV B and the non-normal–nonlinear nature of the transition in Sec. IV C. The paper concludes in Sec. V.

II. GOVERNING EQUATIONS AND NUMERICAL METHODS

We numerically solve the imcompressible Navier-Stokes equations under Boussinesq approximation ($\Delta\rho/\rho_0 \ll 1$). The flow is incompressible, $\boldsymbol{\nabla}\cdot\boldsymbol{u} = 0$, and momentum and density transport equations are

$$\partial_t \boldsymbol{u} + (\boldsymbol{u}\cdot\boldsymbol{\nabla})\boldsymbol{u} = -\boldsymbol{\nabla} p/\rho_0 + \nu\boldsymbol{\nabla}^2\boldsymbol{u} + (\rho-\rho_0)g\hat{\boldsymbol{e}}_\theta/\rho_0, \tag{3a}$$

$$\partial_t \rho + (\boldsymbol{u}\cdot\boldsymbol{\nabla})\rho = \kappa\boldsymbol{\nabla}^2\rho, \tag{3b}$$

where $\boldsymbol{u} = (u_x, u_y, u_z)$ is the velocity field. The coordinates are defined such that the x axis is aligned streamwise along the duct, the y axis spanwise across the duct, and the z axis normal to the duct, making an angle θ with the gravitational vector $\boldsymbol{g} = g\hat{\boldsymbol{e}}_\theta = g(\sin\theta, 0, -\cos\theta)$. The duct streamwise aspect ratio (length/height) is 30 and the spanwise aspect ratio (width/height) is 1, as in most previous experimental and numerical studies. The boundary conditions are no slip for velocity and no flux for density at the four duct walls in y and z.

The partial differential equations are solved with AFiD, a highly parallel solver with a second-order advanced finite difference scheme for spatial derivatives and a third-order Runge-Kutta scheme for time integration [43,44]. We follow the methodology introduced in Ref. [15], using immersed boundary methods (IBMs) to replicate the duct-reservoir geometry [Figs. 2(a)–2(e)] and artificial forces to allow for arbitrarily long runtime with modest domain size. For simulations at higher Ra, we remove the IBM boundary [Fig. 2(f)] to use a wall-clustered mesh in the z direction to fully resolve the turbulent kinetic BLs [45]. Additionally, we use a multiple-resolution technique to resolve ρ for $\mathrm{Pr} = 7$ on a refined uniform mesh via a four-point Hermite interpolation method [46]. With the same duct geometry and Pr as in the previous experimental [12] and numerical studies [15], our simulations successfully reproduce the four qualitative flow regimes at the same control parameters Ra and θ [see Fig. 2(g)]. In the overlapping region of parameter space, our results align closely with previous studies. For further details of the DNS, we refer to the Appendix.

III. GLOBAL TRANSPORT AND FLOW PROPERTIES

A. Mass flux

We begin by examining the primary observable of interest, the scalar transfer efficiency between the two reservoirs, quantified by the Nusselt number (the ratio of total transfer to purely conductive transfer; also called Sherwood number when referring to mass transfer):

$$\mathrm{Nu} \equiv \frac{\langle u_x(\rho-\rho_0)\rangle}{\kappa\Delta\rho/H} + 1, \tag{4}$$

where $\langle\cdot\rangle$ denotes the volume and time average over the duct region of volume $V = 28H^3$ between the dashed black lines in Figs. 2(a)–2(f). In Fig. 3(a), we present Nu as function of Ra in the range $\mathrm{Ra} \in [6\times10^6, 2\times10^9]$ for three angles $\theta = \{4^\circ, 7^\circ, 10^\circ\}$. Our results reveal two scaling regimes. For $\mathrm{Ra} \lesssim 10^8$, the data are consistent with a scaling of $\mathrm{Nu} \sim \mathrm{Ra}^{1/3}$, as expected for weakly driven thermal convection [28]. Beyond $\mathrm{Ra} \approx 10^8$, the system undergoes a transition to the ultimate regime where the mass transfer efficiency follows the enhanced scaling $\mathrm{Ra}^{1/2}$.

The transition is more apparent in Fig. 3(b), where Nu is compensated by $\mathrm{Ra}^{1/3}$. In the low-Ra regime, data points scatter around the horizontal dashed gray line corresponding to $\mathrm{Nu} \sim \mathrm{Ra}^{1/3}$, close to the effective scaling $\mathrm{Nu} \sim \mathrm{Ra}^{0.3}$ reported in Ref. [32] for weakly turbulent CVC. Here, turbulence is not fully developed (or transitional) and SID flow is affected by a family of linear

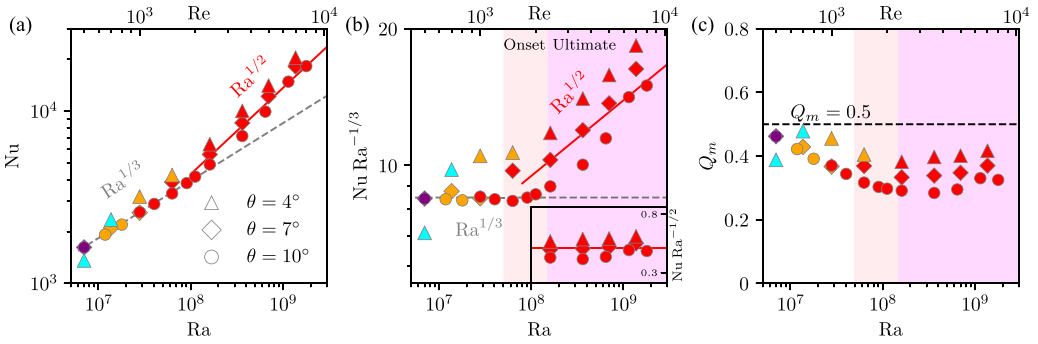

FIG. 3. (a) Log-log plot of Nu against Ra. The fill color represents the flow regime as indicated in Fig. 2(g) and the shape corresponds to the inclination. The slope for small Ra is consistent with $\mathrm{Nu} \sim \mathrm{Ra}^{1/3}$ (dashed line). Scaling in the ultimate regime is guided by the red line, $\mathrm{Ra}^{1/2}$. (b) Same data as (a), but compensated by $\mathrm{Ra}^{1/3}$. The inset shows the data in the ultimate regime compensated by $\mathrm{Ra}^{1/2}$. (c) Hydraulic dimensionless mass flux Q_m against Ra; the vertical scale is linear. The dashed line marks the hydraulic limit $Q_m = 0.5$.

instabilities as reported in Refs. [47,48]; i.e., the first two points of $\theta = 4°$ deviate noticeably because the bulk flow structures are still laminar, as indicated by the fill color and flow visualization in Fig. 2. The $\theta = 10°$ data follow the $\mathrm{Nu} \sim \mathrm{Ra}^{1/3}$ scaling most closely, likely because the larger angle more closely resembles RB convection and CVC. Castaing *et al.* [32,33] attributed this regime to the absence of Kolmogorov inertial range, yet scalar turbulence is already developed for $\mathrm{Pr} > 1$. Near the onset [highlighted by orange shading in Fig. 3(b)], the scaling departs from $\mathrm{Ra}^{1/3}$, and in the ultimate regime (magenta shading), data align with the red line, $\mathrm{Nu} \sim \mathrm{Ra}^{1/2}$, for all three angles, highlighted in the inset. The ultimate regime reflects that the transport is independent of ν and κ. Under this assumption, the scaling is obtained by simple dimensional analysis [42]. We emphasize that the scaling is steeper than in the beginning of the ultimate regime of RB convection, where the logarithmic corrections from the turbulent thermal BLs yield an effective $\mathrm{Nu} \sim \mathrm{Ra}^{0.38}$ scaling [28]. In contrast, in SID flow, thermal BLs are eliminated by the reservoirs, and the entire channel is analogous to homogeneous RB flow [31].

We now turn our attention to the hydraulic dimensionless mass flux,

$$Q_m \equiv \frac{2\langle u_x(\rho - \rho_0)\rangle}{U_0\,\Delta\rho} = \frac{2(\mathrm{Nu} - 1)}{(\mathrm{Ra}\,\mathrm{Pr})^{1/2}}, \tag{5}$$

a metric widely used in the hydraulics and stratified flow communities. According to classical hydraulic control theory for two-layer steady exchange flows, $Q_m \to 1/2$ in the inviscid limit $\mathrm{Re}, \mathrm{Ra} \to \infty$ [1,49–51]. Figure 3(c) reveals a nonmonotonic dependency of Q_m on Ra. In the low-Ra regime, Q_m approaches its maximal value of about 0.5, where the turbulence- or wave-driven exchange of the scalar across the density interface is minimal. As Ra increases, the flow becomes more turbulent and mixed, and Q_m decreases. It eventually plateaus in the ultimate regime toward a constant well below 0.5. Similar behavior has been documented in SID experiments with salt ($\mathrm{Pr}_s \approx 700$), where our Re values and theirs are comparable, but their values of Ra, $\mathrm{Ra} \approx 10^9$–10^{11}, are two orders of magnitude higher than ours [12]. In those experiments, Q_m converges to a larger asymptotic value close to 0.5 (see their Fig. 6). Our data suggest a slight logarithmic uptrend in the ultimate regime, possibly hinting at $Q_m \to 0.5$ as $\mathrm{Ra} \to \infty$. On the other hand, the $\mathrm{Nu} \sim \mathrm{Ra}^{1/2}$ scaling is an upper bound for turbulent convection at finite Pr [28,52], implying that Q_m is independent of Ra in the ultimate regime. Further investigation into the asymptotic behavior at large Ra and Re, as well as the influence of Pr, would be valuable to better understand the (dis)similarities between SID flow and the broader class of wall-bounded turbulent convection.

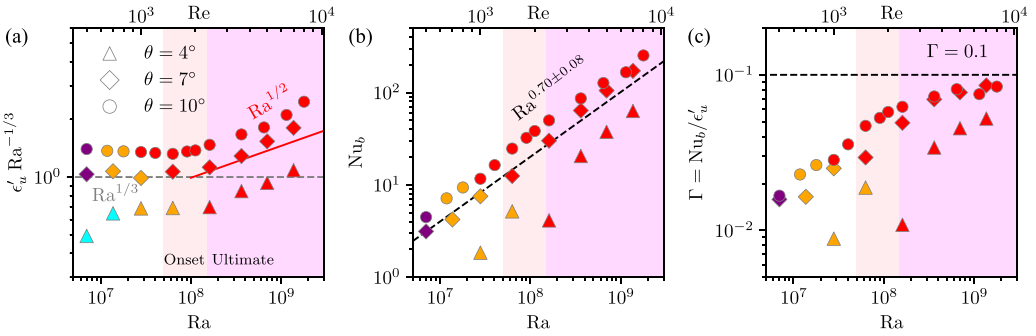

FIG. 4. (a) Log-log plot of the dimensionless dissipation $\epsilon'_u = \langle\epsilon_u\rangle \frac{H^4\mathrm{Pr}^2}{\nu^3\mathrm{Ra}}$ as a function of Ra, compensated by $\mathrm{Ra}^{1/3}$. The dashed line guides the scaling of $\mathrm{Ra}^{1/3}$ and the solid red line the ultimate $\mathrm{Ra}^{1/2}$. (b) The buoyancy flux Nu_b plotted against Ra. The dashed line guides the measured slope of $\mathrm{Nu}_b \sim \mathrm{Ra}^{0.70}$. (c) The mixing efficiency $\Gamma = \mathrm{Nu}_b/\epsilon'_u$. The dashed line suggests the asymptotic value of $\Gamma = 0.1$. The first two laminar data points for $\theta = 4°$ are excluded from (b) and (c).

B. Mixing and energy budget

In contrast to RB convection, where the relation between Nu and the kinetic energy dissipation $\langle\epsilon_u\rangle \equiv \nu\langle|\nabla\mathbf{u}|^2\rangle$ is exact and closed [28], such a relation exists neither in SID nor in vertical convection [34]. The energy budget equation is

$$\langle\epsilon_u\rangle - \Phi_u = \frac{\nu^3}{H^4}\frac{\mathrm{Ra}}{\mathrm{Pr}^2}[\sin\theta\,(\mathrm{Nu}-1) - \cos\theta\,(\mathrm{Nu}_b - 1)], \tag{6}$$

where

$$\mathrm{Nu}_b \equiv \frac{\langle u_z(\rho-\rho_0)\rangle}{\kappa\Delta\rho/H} + 1 \tag{7}$$

is the buoyancy flux quantifying vertical mixing in the duct's frame of reference and $\Phi_u = (1/V)\langle u_x|\boldsymbol{u}|^2/2 + u_x p\rangle_A|_{R-L}$ is the net convective momentum flux ($\langle\cdot\rangle_A$ denoting averaging over the duct cross section of H^2 and time, and $\cdot|_{R-L}$ the difference between the right and left duct ends). The dimensionless dissipation

$$\epsilon'_u \equiv \langle\epsilon_u\rangle\frac{H^4\mathrm{Pr}^2}{\nu^3\mathrm{Ra}}, \tag{8}$$

shown in Fig. 4(a), exhibits a steeper Ra scaling in the ultimate regime, with $\epsilon'_u \sim \mathrm{Ra}^{1/3}$ before and $\epsilon'_u \sim \mathrm{Ra}^{1/2}$ after the transition, reflecting the Nu(Ra) scalings. The edge momentum flux $|\Phi_u| \ll \langle\epsilon_u\rangle$ is very small according to our numerical results and can thus be neglected in Eq. (6) (see Table II in the Appendix). The buoyancy flux Nu_b, shown in Fig. 4(b), exhibits an effective scaling $\mathrm{Nu}_b \sim \mathrm{Ra}^{0.70}$. In contrast to RB convection, where $\mathrm{Nu}_b = 0$ due to homogeneity along the direction normal to the lateral walls, SID stratification leads to a finite buoyancy flux. The negative sign in front of Nu_b in Eq. (6) indicates that the kinetic energy generated by the buoyancy Nu is consumed by both dissipation ϵ_u and mixing Nu_b in the stratified layer. Notably, no clear transition is observed in the $\mathrm{Nu}_b(\mathrm{Ra})$ scaling, consistent with our conjecture that the ultimate transition in SID is associated with the top and bottom wall kinetic BLs (cf. Sec. IV), where $|\partial_z\rho| \approx 0$ and $|u_z| \ll 1$, contributing negligibly to Nu_b.

In Fig. 4(c), we plot the ratio

$$\Gamma \equiv \frac{\mathrm{Nu}_b}{\epsilon'_u}, \tag{9}$$

commonly referred to as the flux parameter, a key quantity in the ocean mixing literature [53] that characterizes mixing efficiency—essentially quantifying the "taxation" of stratification on turbulent dissipation [54]. We observe that Γ increases from approximately 0.01 and appears to asymptote to approximately 0.1 at large Ra for all three angles θ. The value aligns with previous stratified turbulence DNSs in a triply periodic domain [55] and with previous SID experiments [14] and DNSs [15]. Notably, it is significantly lower than the widely adopted $\Gamma \approx 0.2$ in the oceanography literature [53,54,56] for reasons that remain to be understood.

C. Analogy to convection in a vertical channel

We now seek to understand the origin of the observed ultimate scaling $\mathrm{Nu} \sim \mathrm{Ra}^{1/2}$ through the analogy to CVC, where this scaling is widely reported due to a linear density gradient driving the turbulence [32,33,61]. We plot the streamwise dimensionless density (or buoyancy) profiles $\frac{\langle \rho - \rho_0 \rangle_{y,z,t}}{\Delta\rho}(x)$ for $\theta = 7^\circ$ in Fig. 5(a), where $\langle \cdot \rangle_{y,z,t}$ denotes averaging over y, z, and time. As Ra increases, these profiles become linear in x with a slope of approximately 0.01. In Fig. 5(b), we show the measured dimensionless mean density gradient,

$$\beta \equiv H \frac{\mathrm{d}}{\mathrm{d}x}\left(\frac{\langle \rho - \rho_0 \rangle_{y,z,t}}{\Delta\rho}\right), \tag{10}$$

for all three angles θ, where the asymptotic value of β approaches 0.01 regardless of θ. The interpretation is that, as mixing develops within the duct, turbulent convection becomes dominant in the ultimate regime, sustained by the streamwise linear density gradient, resulting in the $\mathrm{Nu} \sim \mathrm{Ra}^{1/2}$ scaling consistent with CVC. At lower Ra where turbulence is not fully developed, we observe that some cases exhibit negative density gradients ($\beta < 0$). These flows are hydraulically subcritical, as explained by hydraulic control theory [11], primarily governed by interfacial waves and linear instabilities [as visualized in Figs. 2(b)–2(d)], rather than by turbulent convection.

To quantify the effective buoyancy driving strength in the duct, we define a Grashof number based on the mean density gradient β:

$$\mathrm{Gr} \equiv \beta \frac{g(\Delta\rho/\rho_0)H^3}{\nu^2} = \beta \frac{\mathrm{Ra}}{\mathrm{Pr}}. \tag{11}$$

In Fig. 5(c), we plot our DNS results alongside previous experimental [32,57–62] and numerical [31] studies of CVC, where Nu is compensated by Pr^{-1} and $(L/H)\sin\theta$ (the effective nondimensional transport distance along gravity). All data follow a similar $\mathrm{Gr}^{1/2}$ scaling toward the ultimate regimes, though the effective scalar transport decreases significantly for $\theta = 90^\circ$. SID flow exhibits higher scaling prefactors possibly due to the mean velocity gradient aligning with the stratification, approximating a two-layer configuration and thereby enhancing the transport. Interestingly, the onset $\mathrm{Gr} \approx 10^5$ appears to be universal for both SID flow (small θ) and CVC ($\theta = 90^\circ$). We further present two additional sets of simulations at $\theta = 45^\circ$ and 90°, shown as black markers in Fig. 5(c). For these large inclinations, the stratification is weak or absent and the system approaches CVC. Notice that in Refs. [31,32,57–62] the length scale in Nu is the duct length L. We use the duct height H instead in this work. Our $\theta = 90^\circ$ data collapse nicely with the CVC data after being compensated by the duct aspect ratio $L/H = 30$.

Despite similarities in highly turbulent regimes, the routes to turbulence in the two systems are fundamentally different. CVC transitions through a series of exponentially growing unstable elevator modes [31,63]. In contrast, the transition of SID flow is initially associated with supercritical bifurcations by a family of linear instabilities of the stratified shear layer [47,48]. Lefauve [18] further hypothesized the existence of a subcritical route from intermittency to fully developed turbulence, similar to other initially supercritical systems like RB and Taylor-Couette flow. In the remainder of this paper, we present evidence supporting this subcritical route to ultimate turbulence mediated by turbulence developing within the kinetic BLs.

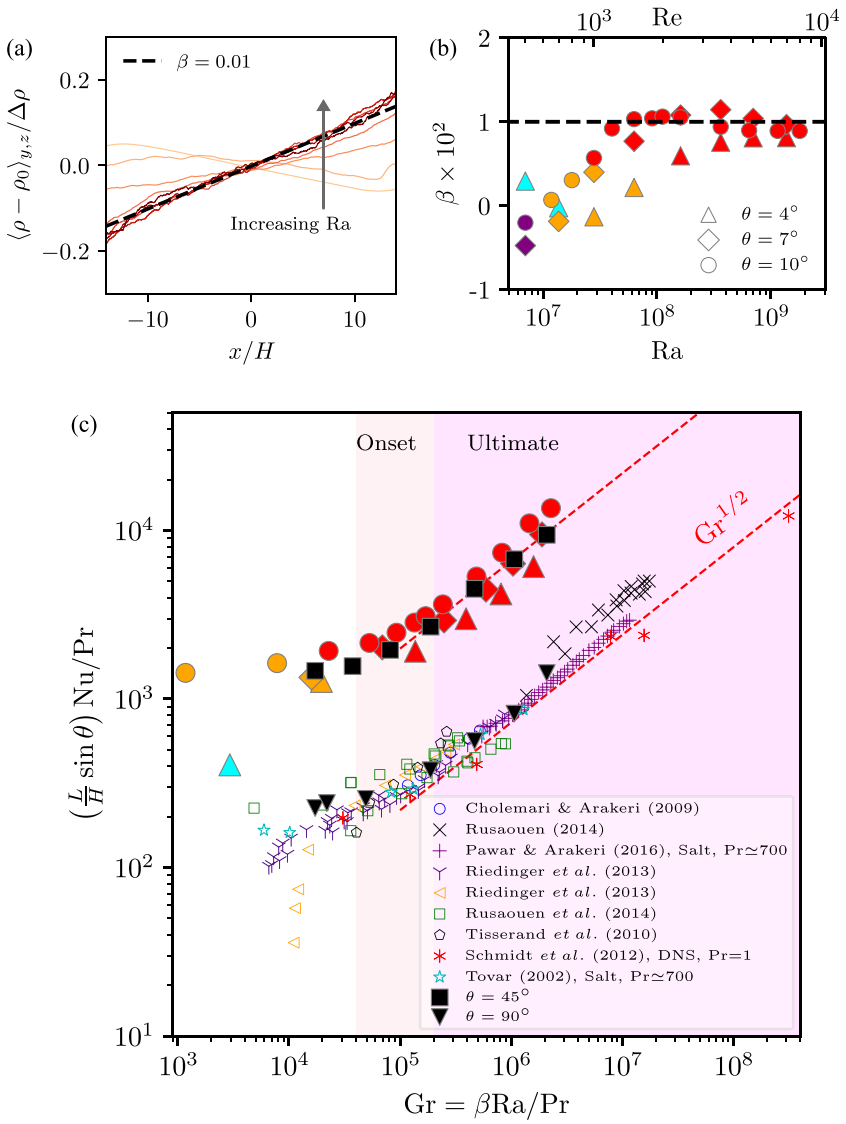

FIG. 5. (a) Mean streamwise density profiles in $x/H \in [-14, 14]$ of $\theta = 7°$, satisfying $(\rho|_{x\approx\pm 20H} - \rho_0)/\Delta\rho = \pm 0.5$ in the reservoirs. Deeper shade of color indicates higher Ra. (b) Density gradient β for all three angles. The dashed lines in (a) and (b) mark the asymptotic value of $\beta = 0.01$ at large Ra. (c) Current SID DNS results (large colored markers, showing only data with positive β) compared with previous CVC data from the literature ($\theta = 90°$) [31,32,57–62] and our additional results of large inclinations (black markers). Previous data are from experiments with heat in water ($\mathrm{Pr} \approx 7$), unless otherwise indicated in the legend. The vertical axis is compensated by $(L/H)\sin\theta\,\mathrm{Pr}^{-1}$.

IV. TURBULENT BOUNDARY LAYERS AND TRANSITION

A. Shear Reynolds number

The key parameter to characterize the transition of kinetic BL structure is the shear Reynolds number,

$$\mathrm{Re}_s \equiv \frac{\max\langle u_x\rangle_{x,y,t}\delta^*}{\nu}, \tag{12}$$

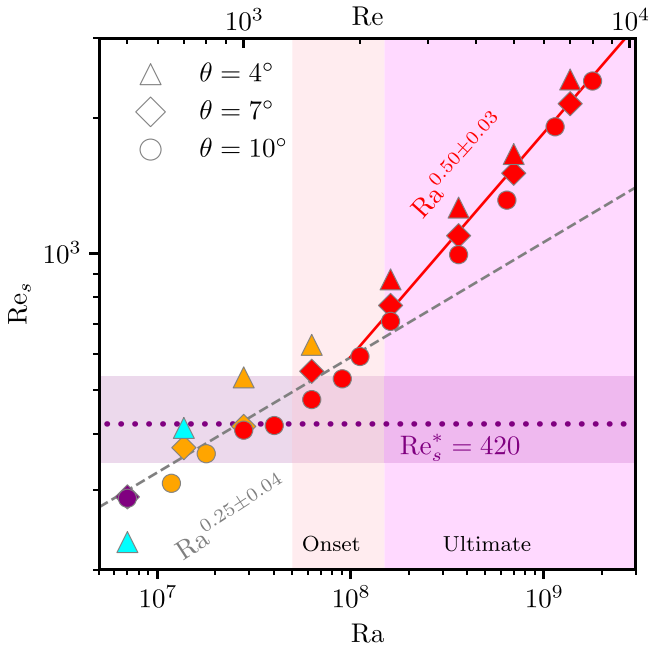

FIG. 6. Log-log plot of shear Reynolds number Re_s against Ra. The purple horizontal dotted line and strip mark $\mathrm{Re}_s^* = 420$, around which the laminar BLs are expected to become turbulent, emphasizing the subcritical nature of the transition, which occurs over a range of Re_s. The fitted slopes match the expected $\mathrm{Re}_s \sim \mathrm{Ra}^{1/4}$ (dashed) for the laminar BL and $\mathrm{Re}_s \sim \mathrm{Ra}^{1/2}$ (solid red) for the turbulent BL.

based on the displacement BL thickness $\delta^* = \int_0^{z_{\max}} (1 - \frac{\langle u_x \rangle_{x,y,t}(z)}{\max \langle u_x \rangle_{x,y,t}})\, \mathrm{d}z$ [64], where $z_{\max}$ corresponds to the location of $\max \langle u_x \rangle_{x,y,t}$, associated with the BLs on top and bottom walls. In Fig. 6, we plot Re_s as a function of Ra. In the low-Ra regime, we find that the measured slope, $\mathrm{Re}_s \sim \mathrm{Ra}^{0.25} \sim \mathrm{Re}^{0.5}$, matches with the expected scaling based on the laminar BL thickness $\delta^*/H \sim \mathrm{Ra}^{-1/4} \sim \mathrm{Re}^{-1/2}$. In the ultimate regime, the scaling shifts to $\mathrm{Re}_s \sim \mathrm{Ra}^{1/2} \sim \mathrm{Re}$ for turbulent BLs. Landau and Lifshitz [64] reported the estimate of $\mathrm{Re}_s^* \approx 420$ for the range of the transition to a turbulent BL (a detailed discussion can be found in Ref. [28]). We observe that indeed $\mathrm{Re}_s \gtrsim 420$ coincides with the onset region (highlighted in orange) where the Nu scaling changes [Figs. 3(a) and 3(b)]. This suggests that the transition to ultimate turbulence may be caused by changes in the BLs, although a coincidence cannot be ruled out.

B. Streamwise velocity profiles

A hallmark feature of a turbulent BL is the logarithmic law of the wall. We plot the averaged streamwise velocity profiles near $z = 0$ (bottom wall) at $y = H/2$ (spanwise midplane) in Fig. 7(a). The profiles are shown in the wall-normal units with $u^+ \equiv \langle u_x \rangle_{x,t}/u_\tau$, where $u_\tau = \sqrt{\nu \partial_z \langle u_x \rangle_{x,t}|_{z=0}}$ is the friction velocity, and the spatial coordinates $z^+ \equiv z/\delta_\nu$, with $\delta_\nu = \nu/u_\tau$ being the viscous unit. The magenta curves mark the profiles near the ultimate transition where the BLs have just turned turbulent. At large Ra, we notice that the curves converge to the shape of canonical 3D wall turbulence, comprising the viscous linear sublayer and by the short logarithmic region $u^+ = (1/\kappa_\nu) \ln z^+ + B$ with $\kappa_\nu = 0.41$ agreeing with the von Kármán constant. The parameter B differs slightly for different θ. We note that the logarithmic regions are not fully developed even at our highest Ra, spanning only about half a decade in z^+. This is not surprising: in SID flow, the logarithmic region is immediately followed by a negative mean velocity gradient in the bulk,

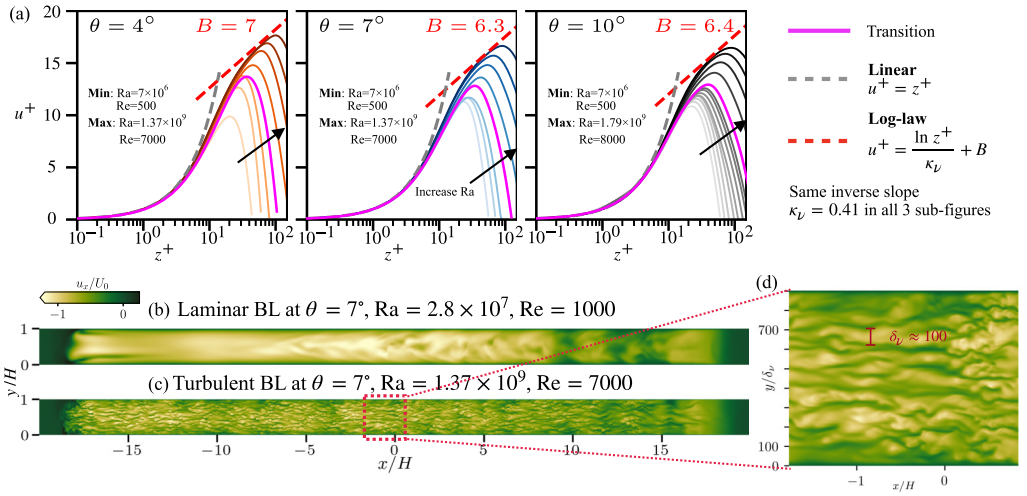

FIG. 7. (a) Overall streamwise velocity $\langle u_x|_{y=H/2}\rangle_{x,t}(z)$ profiles in wall-normal units. Deeper colors represent higher Ra. The dashed lines correspond to the canonical 3D wall-bounded turbulence profile: the linear viscous sublayer (gray), and the logarithmic law with inverse slope $\kappa_v = 0.41$ (red); B varies slightly for different θ. [(b)–(d)] Flow visualization (bottom view) of streamwise velocity u_x at $z \approx 12\delta_v$ (b) inside the BL before the transition and (c) after the transition, expanded in (d). The y axes are scaled up by 2 in (b)–(d).

arising from the counterdirectional nature of the exchange flows, rather than by the free-streaming wake region of canonical turbulent boundary layers. This likely suppresses the logarithmic law from extending further into z^+.

To further appreciate the features in the BLs in different regimes, we plot snapshots of the streamwise velocity u_x near the buffer layer $z^+ \approx 12$. The laminar BL in Fig. 7(b) exhibits an overall smooth profile, with disturbances being generated upstream and dissipated downstream. The turbulent BL in Fig. 7(c) is qualitatively different, exhibiting meandering streaks across the entire duct. These streaks are another hallmark of turbulent BLs, well documented in canonical turbulent BL literature [65]. In the expanded view in Fig. 7(d), we observe that the spanwise spacings of these streaks are around 100–200 viscous units, consistent with previous studies on wall turbulence [65,66].

C. Nature of the transition to ultimate SID

The non-normal–nonlinear nature of the transition is demonstrated in Fig. 8. We run two time-dependent realizations spanning the onset and ultimate range, $\mathrm{Ra} \approx 5.5 \times 10^7$ to 2.5×10^8 [$\mathrm{Re} \approx 1400$–3200; see Fig. 3(b)]. Starting in the intermittent regime, the compensated transport $\mathrm{Nu}(t)/\sqrt{\mathrm{Ra}(t)\mathrm{Pr}}$ shows strong intermittency, with peaks during the quiet phase [Fig. 2(c)] and valleys during the active phase [Fig. 2(d)]. As Ra is slowly increased toward approximately 2.5×10^8 (black curve), the fluctuations decrease significantly, marking the entry into the ultimate regime. During the ramp down, however, the ultimate regime persists until a much lower $\mathrm{Ra} \approx 1.5 \times 10^8$, after which intermittency reappears. The second realization (gray) transitions at different Ra, and the up- and down-ramp thresholds also differ from each other. This realization dependence and hysteresis reflect that there is no single sharp Ra for the ultimate regime, and thus that the transition is subcritical and hysteretic.

Linear stability analysis suggests SID flow becomes linearly unstable for $\mathrm{Re} \lesssim 650$, $\mathrm{Ra} \lesssim 1.2 \times 10^6$ [48], well below the observed turbulent BL and ultimate transition. This finding suggests that the nonlinear subcritical shear instability developed within the BLs is crucial to trigger ultimate

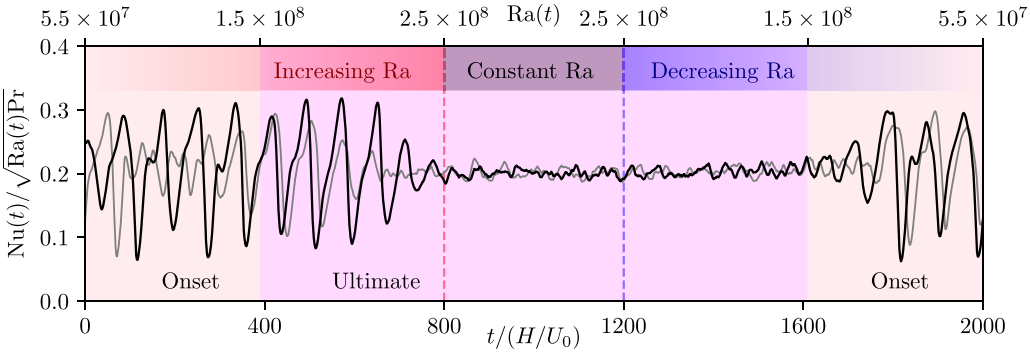

FIG. 8. Hysteresis of the instantaneous Nu (compensated by $\sqrt{\mathrm{RaPr}}$) plotted against dimensionless time. The upper axis shows the imposed $\mathrm{Ra}(t)$: a slow linear ramp up, a constant hold, and an equally slow ramp down. Two independent realizations at $\theta = 4^\circ$ are shown (black and gray). The up and down ramps span the transition Ra range toward the ultimate SID regime, and the regime colors match Fig. 3(b).

turbulent convection in SID flow. This contrasts with homogeneous RB convection [31], where no evidence of turbulent BLs on the lateral walls has been reported.

V. CONCLUSIONS AND OUTLOOK

In this work, we presented a 3D DNS of SID flow in the ultimate regime. The transition at $\mathrm{Ra} \approx 10^8$ is marked by an enhancement in mass transfer efficiency to the asymptotic ultimate scaling of $\mathrm{Nu} \sim \mathrm{Ra}^{1/2}$. We interpret this as the point where turbulent convection becomes the dominant driving mechanism, sustained by the formation of a streamwise uniform density gradient, analogous to the behavior observed in homogeneous RB convection. Simultaneously, the shear Reynolds number at the top and bottom walls exceeds $\mathrm{Re}_s^* \approx 420$, triggering turbulent BLs through a non-normal–nonlinear subcritical route. The Ra range for the onset of the ultimate regime coincides with the turbulent BL transition, independently of the duct inclination θ, despite clear variations in global flow regimes with θ, supporting the interpretation that the transition is associated with the BLs. From a broader fluid dynamics perspective, SID flow offers a distinct internal wall shear flow configuration characterized by two extrema in the mean velocity profile, contrasting with canonical wall turbulence, which exhibit either no extremum (plane Couette) or a single extremum (Poiseuille).

Many questions remain open. Although the asymptotic $Q_m = 1/2$ predicted by inviscid two-layer hydraulics coincides with the scaling $\mathrm{Nu} \sim \mathrm{Ra}^{1/2}$, our results show that $Q_m < 0.5$ in the current range of $\mathrm{Ra} \approx 10^7$–10^9. It remains unclear whether Q_m will remain below 0.5 indefinitely or eventually approach 0.5 as $\mathrm{Ra} \to \infty$. Furthermore, our current interpretation is unlikely to hold for very small θ or in a horizontal duct ($\theta \approx 0^\circ$), where the streamwise convective driving is weak or absent compared to horizontal hydrostatic pressure, even in the turbulent regime. Whether horizontal SID flow can exhibit the ultimate regime remains to be investigated.

Our results highlight universalities among various wall-bounded convective flows. Beyond fundamental fluid dynamics, our scaling laws for turbulent transport and energetics, including mixing efficiency, may help inform high-Re and high-Ra closure models in geophysics and engineering.

ACKNOWLEDGMENTS

We thank Dr. C. Howland, G. Vacca, and Dr. K. Zhong for fruitful discussions on numerical techniques and boundary layers and Professor J. Salort for sharing data of convection in a vertical channel. A.L. was supported by a NERC Independent Research Fellowship (No. NE/W008971/1). We acknowledge the EuroHPC Joint Undertaking for awarding Grant No. EHPCREG-2023R03-178

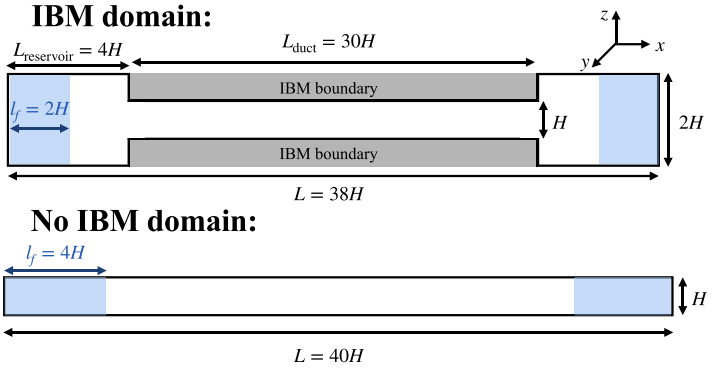

FIG. 9. Sketch of simulation domain geometry. Both geometries have thickness H in the y direction. Please note the figures are not to scale.

CPU hours on the EuroHPC supercomputer Discoverer at the Sofia Tech Park in Bulgaria; the project "2024.056-Convection and phase-change in turbulent geophysical flows" of the research program "Computing Time on National Computing Facilities" co-funded by the Dutch Research Council (NWO); and the Gauss Center for Supercomputing e.V. for project ID pr74sa on the GCS Supercomputer SuperMUC-NG at the Leibniz Supercomputing Center. A.L. and D.L. also acknowledge the NSF- and ONR-funded Geophysical Fluid Dynamics Program at the Woods Hole Oceanographic Institution, where this work was initiated.

DATA AVAILABILITY

Due to the large size of the simulation output files, the original flow-field data are not publicly available, but can be provided by the authors upon request. The measurement data are included in the Appendix.

APPENDIX: NUMERICAL DETAILS AND DATA

We solved the following nondimensionalized equations which are the basis for the numerical simulations:

$$\boldsymbol{\nabla}\cdot\boldsymbol{u} = 0, \tag{A1a}$$

$$\partial_t\boldsymbol{u} + (\boldsymbol{u}\cdot\boldsymbol{\nabla})\boldsymbol{u} = -\boldsymbol{\nabla}p + \sqrt{\frac{\mathrm{Pr}}{\mathrm{Ra}}}\boldsymbol{\nabla}^2\boldsymbol{u} + \rho\hat{\boldsymbol{e}}_\theta - \boldsymbol{F}_u, \tag{A1b}$$

$$\partial_t\rho + (\boldsymbol{u}\cdot\boldsymbol{\nabla})\rho = \sqrt{\frac{1}{\mathrm{PrRa}}}\boldsymbol{\nabla}^2\rho - F_\rho. \tag{A1c}$$

Following Ref. [15], the artificial restoring forces $\boldsymbol{F}_u$ and F_ρ are given by

$$\boldsymbol{F}_u \equiv F_u\boldsymbol{u} \equiv \left[\frac{1-\tanh\left(\frac{8}{l_f}\left(x+\frac{L-l_f}{2}\right)\right)}{\eta_u} + \frac{1+\tanh\left(\frac{8}{l_f}\left(x-\frac{L-l_f}{2}\right)\right)}{\eta_u}\right]\boldsymbol{u}, \tag{A2}$$

$$F_\rho \equiv \frac{1-\tanh\left(\frac{8}{l_f}\left(x+\frac{L-l_f}{2}\right)\right)}{\eta_\rho}\left(\rho-\frac{1}{2}\right) + \frac{1+\tanh\left(\frac{8}{l_f}\left(x-\frac{L-l_f}{2}\right)\right)}{\eta_\rho}\left(\rho+\frac{1}{2}\right). \tag{A3}$$

where l_f is the streamwise length of influence of the forcing and L is the simulation domain length in x. The parameters η_u and η_ρ control the restoring force strength. The parameters used for each simulation are provided in Table I.

TABLE I. Values of the control parameters and resolutions of the simulations. N_z is the velocity field resolution in the vertical direction (normal to the duct), N_x streamwise, and N_y spanwise. N^r is the refined resolution for scalar field ρ. N_{BL} is number of grid points in the boundary layer. Δz_1^+ is the distance of the first grid point from the wall in wall-normal units. Letters in the last column: L: Laminar, W: Wave, I: Intermittent Turbulence, T: Turbulence, cf. Figs. 2(a)–2(e).

θ	Ra	Re	IBM	$N_z \times N_x \times N_y$	$N_z^r \times N_x^r \times N_y^r$ (uniform)	N_{BL}	Δz_1^+	L	l_f	η_u	η_ρ	Regime
10°	7×10^6	500	Yes	$256 \times 2048 \times 128$ (Uniform)	$256 \times 2048 \times 128$	23	0.42	38	2	10	0.2	W
10°	1.18×10^7	650	Yes	$256 \times 2048 \times 128$ (Uniform)	$256 \times 2048 \times 128$	20	0.50	38	2	10	0.2	I
10°	1.79×10^7	800	Yes	$256 \times 2048 \times 128$ (Uniform)	$256 \times 2048 \times 128$	19	0.59	38	2	10	0.2	I
10°	2.8×10^7	1000	Yes	$256 \times 2048 \times 128$ (Uniform)	$256 \times 2048 \times 128$	17	0.70	38	2	10	0.2	T
10°	4.03×10^7	1200	Yes	$256 \times 3072 \times 128$ (Uniform)	$256 \times 3072 \times 128$	15	0.81	38	2	10	0.2	T
10°	6.3×10^7	1500	Yes	$256 \times 3072 \times 128$ (Uniform)	$256 \times 3072 \times 128$	14	0.96	38	2	10	0.2	T
10°	9.07×10^7	1800	Yes	$384 \times 3072 \times 128$ (Uniform)	$384 \times 3072 \times 128$	19	0.75	38	2	10	0.2	T
10°	1.12×10^8	2000	Yes	$384 \times 3072 \times 128$ (Uniform)	$384 \times 3072 \times 128$	19	0.81	38	2	10	0.2	T
10°	1.61×10^8	2400	Yes	$512 \times 4096 \times 192$ (Uniform)	$512 \times 4096 \times 192$	24	0.70	38	2	10	0.2	T
10°	3.63×10^8	3600	Yes	$768 \times 6144 \times 256$ (Uniform)	$768 \times 6144 \times 256$	32	0.66	38	2	10	0.2	T
10°	1.61×10^8	2400	No	$256 \times 4096 \times 256$ (z wall clustered)	$256 \times 4096 \times 256$	41	5.03×10^{-3}	40	4	5	0.5	T
10°	3.63×10^8	3600	No	$512 \times 6144 \times 384$ (z wall clustered)	$512 \times 6144 \times 384$	71	2.36×10^{-3}	40	4	5	0.5	T
10°	6.45×10^8	4800	No	$512 \times 6144 \times 384$ (z wall clustered)	$512 \times 6144 \times 384$	68	2.75×10^{-3}	40	4	5	0.5	T
10°	1.15×10^9	6400	No	$768 \times 8192 \times 512$ (z wall clustered)	$768 \times 8192 \times 512$	100	1.91×10^{-3}	40	4	5	0.5	T
10°	1.79×10^9	8000	No	$768 \times 8192 \times 512$ (z wall clustered)	$768 \times 8192 \times 512$	99	2.21×10^{-3}	40	4	5	0.5	T
7°	7×10^6	500	No	$96 \times 1024 \times 64$ (z wall clustered)	$192 \times 2048 \times 128$	27	2.03×10^{-2}	40	4	5	0.5	W
7°	1.32×10^7	700	No	$96 \times 1024 \times 64$ (z wall clustered)	$192 \times 2048 \times 128$	26	2.42×10^{-2}	40	4	5	0.5	I
7°	2.8×10^7	1000	No	$128 \times 1536 \times 96$ (z wall clustered)	$256 \times 3072 \times 192$	30	1.84×10^{-2}	40	4	5	0.5	I
7°	6.3×10^7	1500	No	$128 \times 1536 \times 96$ (z wall clustered)	$256 \times 3072 \times 192$	27	2.21×10^{-2}	40	4	5	0.5	T
7°	1.61×10^8	2400	No	$192 \times 2048 \times 128$ (z wall clustered)	$384 \times 4096 \times 256$	34	1.44×10^{-2}	40	4	5	0.5	T
7°	3.63×10^8	3600	No	$192 \times 2048 \times 128$ (z wall clustered)	$384 \times 4096 \times 256$	32	1.69×10^{-2}	40	4	5	0.5	T
7°	7×10^8	5000	No	$256 \times 3072 \times 192$ (z wall clustered)	$512 \times 6144 \times 384$	39	1.33×10^{-2}	40	4	5	0.5	T
7°	1.37×10^9	7000	No	$256 \times 3072 \times 192$ (z wall clustered)	$512 \times 6144 \times 384$	38	1.45×10^{-2}	40	4	5	0.5	T
4°	7×10^6	500	No	$96 \times 1024 \times 64$ (z wall clustered)	$192 \times 2048 \times 128$	29	2.03×10^{-2}	40	4	5	0.5	L
4°	1.32×10^7	700	No	$96 \times 1024 \times 64$ (z wall clustered)	$192 \times 2048 \times 128$	29	2.42×10^{-2}	40	4	5	0.5	L
4°	2.8×10^7	1000	No	$128 \times 1536 \times 96$ (z wall clustered)	$256 \times 3072 \times 192$	34	1.84×10^{-2}	40	4	5	0.5	I
4°	6.3×10^7	1500	No	$128 \times 1536 \times 96$ (z wall clustered)	$256 \times 3072 \times 192$	31	2.21×10^{-2}	40	4	5	0.5	I
4°	1.61×10^8	2400	No	$192 \times 2048 \times 128$ (z wall clustered)	$384 \times 4096 \times 256$	39	1.44×10^{-2}	40	4	5	0.5	T
4°	3.63×10^8	3600	No	$192 \times 2048 \times 128$ (z wall clustered)	$384 \times 4096 \times 256$	36	1.69×10^{-2}	40	4	5	0.5	T
4°	7×10^8	5000	No	$192 \times 2048 \times 128$ (z wall clustered)	$384 \times 4096 \times 256$	34	1.98×10^{-2}	40	4	5	0.5	T
4°	1.37×10^9	7000	No	$256 \times 3072 \times 192$ (z wall clustered)	$512 \times 6144 \times 384$	43	1.45×10^{-2}	40	4	5	0.5	T

The detailed simulation domain geometry is illustrated in Fig. 9. The z wall-clustered grid scheme for velocity fields in Table I follows Ref. [45]. The time-averaged results are available in Table II. The two data points shown in the main text, $\theta = 10°$, $\mathrm{Ra} = 1.61 \times 10^8$ and $\theta = 10°$, $\mathrm{Ra} = 3.63 \times 10^8$, are the averages of IBM and non-IBM geometry simulation results.

TABLE II. Results from the numerical simulations. The standard deviations σ are computed based on fluctuations over time. Φ_u is computed based on Eq. (6), which is small compared to $\langle\epsilon_u\rangle$, roughly comparable to the standard deviation σ_{ϵ_u}. $\mathrm{Re}_L = \max\langle u_x\rangle_{x,y,t} H/\nu$ is the bulk Reynolds number. τ is the nondimensional time to get the statistics, scaled by $T_0 = H/U_0 = \sqrt{H/g(\Delta\rho/\rho_0)}$.

θ	Ra	Re	Nu	σ_{Nu}	$\frac{\langle\epsilon_u\rangle}{\nu^3 H^{-4}}\frac{\mathrm{Pr}^2}{\mathrm{Ra}}$	σ_{ϵ_u}	$\frac{\langle\Phi_u\rangle}{\nu^3 H^{-4}}\frac{\mathrm{Pr}^2}{\mathrm{Ra}}$	Re_L	Re_s	τ
10°	7×10^6	500	1617.31	±23.03	267.85	±5.02	−8.59	1014.62	287.57	200
10°	1.18×10^7	650	1919.97	±127.42	312.27	±23.47	−14.09	1238.02	310.38	200
10°	1.79×10^7	800	2192.74	±183.20	356.37	±35.77	−15.17	1476.64	360.90	200
10°	2.8×10^7	1000	2591.32	±160.16	410.15	±30.65	−28.36	1882.23	406.79	200
10°	4.03×10^7	1200	2889.55	±36.59	458.19	±8.39	−27.45	2224.87	416.60	200
10°	6.3×10^7	1500	3324.60	±36.60	525.94	±7.52	−27.03	2711.28	475.46	200
10°	9.07×10^7	1800	3818.07	±33.63	611.01	±7.34	−20.18	3242.53	528.55	100
10°	1.12×10^8	2000	4164.90	±26.74	664.13	±5.58	−21.38	3613.27	592.15	100
10°	1.61×10^8	2400	4793.24	±28.41	778.74	±5.75	−5.02	4346.93	689.07	100
10°	3.63×10^8	3600	6851.08	±40.96	1137.68	±10.97	27.69	6696.61	955.65	100
10°	1.61×10^8	2400	4996.74	±117.42	824.72	±34.27	101.11	4360.58	727.45	200
10°	3.63×10^8	3600	7469.28	±120.83	1243.65	±29.72	208.71	6737.19	1034.11	101
10°	6.45×10^8	4800	9914.83	±117.54	1568.99	±97.51	209.02	9129.29	1313.24	50
10°	1.15×10^9	6400	14 802.87	±506.44	2208.70	±185.06	111.04	12 883.95	1908.52	25
10°	1.79×10^9	8000	18 214.52	±729.95	3004.30	±185.77	560.66	16 624.96	2409.56	25
7°	7×10^6	500	1617.83	±82.56	197.81	±9.66	9.64	937.20	289.61	200
7°	1.32×10^7	700	2101.43	±367.52	256.59	±65.02	12.60	1269.85	372.18	200
7°	2.8×10^7	1000	2570.95	±463.44	300.32	±90.33	8.61	1612.27	414.71	400
7°	6.3×10^7	1500	3874.74	±649.94	424.29	±123.86	−12.06	2638.98	549.23	400
7°	1.61×10^8	2400	5599.55	±460.51	611.77	±95.37	15.71	4261.51	768.07	200
7°	3.63×10^8	3600	8531.84	±182.43	918.37	±30.34	62.12	6626.91	1095.74	139
7°	7×10^8	5000	12 165.58	±610.55	1363.96	±166.36	183.37	9562.43	1506.41	83
7°	1.37×10^9	7000	18 127.54	±1279.37	2007.37	±311.96	291.23	14 089.94	2146.70	77
4°	7×10^6	500	1359.54	±1.65	94.20	±0.19	−4.78	656.78	230.06	200
4°	1.32×10^7	700	2344.97	±34.57	154.70	±1.01	−8.69	1162.11	411.52	200
4°	2.8×10^7	1000	3188.56	±312.16	208.25	±28.44	−8.85	1734.70	532.40	400
4°	6.3×10^7	1500	4248.12	±659.02	274.13	±78.71	−7.30	2458.04	628.35	400
4°	1.61×10^8	2400	6420.84	±816.47	379.25	±91.40	−56.75	4041.98	877.18	100
4°	3.63×10^8	3600	10 013.86	±241.19	602.31	±42.37	−36.95	6331.28	1264.48	100
4°	7×10^8	5000	14 046.73	±93.29	827.48	±23.89	−43.99	8994.81	1661.16	100
4°	1.37×10^9	7000	20 416.35	±219.84	1206.43	±39.36	−35.41	12 996.63	2428.80	100

[1] I. R. Wood, A lock exchange flow, J. Fluid Mech. **42**, 671 (1970).

[2] D. L. Wilkinson, Buoyancy driven exchange flow in a horizontal pipe, J. Eng. Mech. **112**, 485 (1986).

[3] M. Deacon, *Scientists and the Sea 1650-1900, a Study of Marine Science* (Academic Press, London, 1971).

[4] H. B. Fischer, Mixing and dispersion in estuaries, Annu. Rev. Fluid Mech. **8**, 107 (1976).

[5] P. MacCready, W. R. Geyer, and H. Burchard, Estuarine exchange flow is related to mixing through the salinity variance budget, J. Phys. Oceanogr. **48**, 1375 (2018).

[6] P. F. Linden, The fluid mechanics of natural ventilation, Annu. Rev. Fluid Mech. **31**, 201 (1999).

[7] O. Reynolds, An experimental investigation of the circumstances which determine whether the motion of water shall be direct or sinuous, and of the law of resistance in parallel channels, Philos. Trans. R. Soc. **174**, 935 (1883).

[8] G. I. Taylor, Effect of variation in density on the stability of superposed streams of fluid, Proc. R. Soc. A **132**, 499 (1931).
[9] C. R. Meyer and P. F. Linden, Stratified shear flow: Experiments in an inclined duct, J. Fluid Mech. **753**, 242 (2014).
[10] S. A. Thorpe, A method of producing a shear flow in a stratified fluid, J. Fluid Mech. **32**, 693 (1968).
[11] A. Lefauve, J. L. Partridge, and P. F. Linden, Regime transitions and energetics of sustained stratified shear flows, J. Fluid Mech. **875**, 657 (2019).
[12] A. Lefauve and P. F. Linden, Buoyancy-driven exchange flows in inclined ducts, J. Fluid Mech. **893**, A2 (2020).
[13] A. Lefauve and P. F. Linden, Experimental properties of continuously forced, shear-driven, stratified turbulence. Part 1. Mean flows, self-organisation, turbulent fractions, J. Fluid Mech. **937**, A34 (2022).
[14] A. Lefauve and P. F. Linden, Experimental properties of continuously forced, shear-driven, stratified turbulence. Part 2. Energetics, anisotropy, parameterisation, J. Fluid Mech. **937**, A35 (2022).
[15] L. Zhu, A. Atoufi, A. Lefauve, J. R. Taylor, R. R. Kerswell, S. B. Dalziel, G. A. Lawrence, and P. F. Linden, Stratified inclined duct: Direct numerical simulations, J. Fluid Mech. **969**, A20 (2023).
[16] A. Lefauve and M. M. P. Couchman, Data-driven classification of sheared stratified turbulence from experimental shadowgraphs, Phys. Rev. Fluids **9**, 034603 (2024).
[17] A. Lefauve, Y. H. M. Cheung, X. Jiang, and M. M. P. Couchman, Routes to stratified turbulence and temporal intermittency revealed by a cluster-based network model of experimental data, Europhys. Lett. **149**, 53001 (2025).
[18] A. Lefauve, Geophysical stratified turbulence and mixing in the laboratory, C. R. Phys. **25**, 479 (2024).
[19] A. Blass, X. Zhu, R. Verzicco, D. Lohse, and R. J. A. M. Stevens, Flow organization and heat transfer in turbulent wall sheared thermal convection, J. Fluid Mech. **897**, A22 (2020).
[20] Q. Zhou, J. R. Taylor, C. P. Caulfield, and P. F. Linden, Diapycnal mixing in layered stratified plane Couette flow quantified in a tracer-based coordinate, J. Fluid Mech. **823**, 198 (2017).
[21] Q. Zhou, J. R. Taylor, and C. P. Caulfield, Self-similar mixing in stratified plane Couette flow for varying Prandtl number, J. Fluid Mech. **820**, 86 (2017).
[22] G. S. Yerragolam, C. J. Howland, R. J. A. M. Stevens, R. Verzicco, O. Shishkina, and D. Lohse, Scaling relations for heat and momentum transport in sheared Rayleigh–Bénard convection, J. Fluid Mech. **1000**, A74 (2024).
[23] C. J. Howland, G. S. Yerragolam, R. Verzicco, and D. Lohse, Turbulent mixed convection in vertical and horizontal channels, J. Fluid Mech. **998**, A48 (2024).
[24] G. Ahlers, S. Grossmann, and D. Lohse, Heat transfer and large scale dynamics in turbulent Rayleigh–Bénard convection, Rev. Mod. Phys. **81**, 503 (2009).
[25] D. Lohse and K.-Q. Xia, Small-scale properties of turbulent Rayleigh–Bénard convection, Annu. Rev. Fluid Mech. **42**, 335 (2010).
[26] F. Chillà and J. Schumacher, New perspectives in turbulent Rayleigh–Bénard convection, Eur. Phys. J. E **35**, 58 (2012).
[27] K.-Q. Xia, Current trends and future directions in turbulent thermal convection, Theor. Appl. Mech. Lett. **3**, 052001 (2013).
[28] D. Lohse and O. Shishkina, Ultimate Rayleigh-Bénard turbulence, Rev. Mod. Phys. **96**, 035001 (2024).
[29] M. G. Visakh and J. H. Arakeri, Convection in slender Rayleigh–Bénard cells is a combination of wall and tube components, J. Fluid Mech. **1016**, A46 (2025).
[30] M. Gibert, H. Pabiou, F. Chillà, and B. Castaing, High-Rayleigh-number convection in a vertical channel, Phys. Rev. Lett. **96**, 084501 (2006).
[31] L. E. Schmidt, E. Calzavarini, D. Lohse, F. Toschi, and R. Verzicco, Axially homogeneous Rayleigh–Bénard convection in a cylindrical cell, J. Fluid Mech. **691**, 52 (2012).
[32] S. S. Pawar and J. H. Arakeri, Two regimes of flux scaling in axially homogeneous turbulent convection in vertical tube, Phys. Rev. Fluids **1**, 042401(R) (2016).
[33] B. Castaing, E. Rusaouën, J. Salort, and F. Chillà, Turbulent heat transport regimes in a channel, Phys. Rev. Fluids **2**, 062801(R) (2017).

[34] C. S. Ng, A. Ooi, D. Lohse, and D. Chung, Vertical natural convection: Application of the unifying theory of thermal convection, J. Fluid Mech. **764**, 349 (2015).
[35] C. S. Ng, A. Ooi, D. Lohse, and D. Chung, Changes in the boundary-layer structure at the edge of the ultimate regime in vertical natural convection, J. Fluid Mech. **825**, 550 (2017).
[36] C. S. Ng, A. Ooi, D. Lohse, and D. Chung, Bulk scaling in wall-bounded and homogeneous vertical natural convection, J. Fluid Mech. **841**, 825 (2018).
[37] Q. Wang, H. Liu, R. Verzicco, O. Shishkina, and D. Lohse, Regime transitions in thermally driven high–Rayleigh number vertical convection, J. Fluid Mech. **917**, A6 (2021).
[38] J. Ke, N. Williamson, S. W. Armfield, and A. Komiya, The turbulence development of a vertical natural convection boundary layer, J. Fluid Mech. **964**, A24 (2023).
[39] B. Dubrulle and F. Hersant, Momentum transport and torque scaling in Taylor-Couette flow from an analogy with turbulent convection, Eur. Phys. J. B **26**, 379 (2002).
[40] B. Eckhardt, S. Grossmann, and D. Lohse, Torque scaling in turbulent Taylor–Couette flow between independently rotating cylinders, J. Fluid Mech. **581**, 221 (2007).
[41] S. Grossmann, D. Lohse, and C. Sun, High–Reynolds number Taylor–Couette turbulence, Annu. Rev. Fluid Mech. **48**, 53 (2016).
[42] R. H. Kraichnan, Turbulent thermal convection at arbitrary Prandtl number, Phys. Fluids **5**, 1374 (1962).
[43] R. Verzicco and P. Orlandi, A finite-difference scheme for three-dimensional incompressible flow in cylindrical coordinates, J. Comput. Phys. **123**, 402 (1996).
[44] E. P. van der Poel, R. Ostilla-Mónico, J. Donners, and R. Verzicco, A pencil distributed finite difference code for strongly turbulent wall-bounded flows, Comput. Fluids **116**, 10 (2015).
[45] A. Ceci and S. Pirozzoli, Natural grid stretching for DNS of compressible wall-bounded flows, J. Comput. Phys.: X **17**, 100128 (2023).
[46] R. Ostilla-Monico, Y. Yang, E. P. van der Poel, D. Lohse, and R. Verzicco, A multiple-resolution strategy for direct numerical simulation of scalar turbulence, J. Comput. Phys. **301**, 308 (2015).
[47] A. Atoufi, L. Zhu, A. Lefauve, J. R. Taylor, R. R. Kerswell, S. B. Dalziel, G. A. Lawrence, and P. F. Linden, Stratified inclined duct: Two-layer hydraulics and instabilities, J. Fluid Mech. **977**, A25 (2023).
[48] L. Zhu, A. Atoufi, A. Lefauve, R. R. Kerswell, and P. F. Linden, Long-wave instabilities of sloping stratified exchange flows, J. Fluid Mech. **983**, A12 (2024).
[49] H. Stommel and H. G. Farmer, Control of salinity in an estuary by a transition, J. Mar. Res. **12**, 13 (1953).
[50] L. Armi, The hydraulics of two flowing layers with different densities, J. Fluid Mech. **163**, 27 (1986).
[51] S. B. Dalziel, Two-layer hydraulics: A functional approach, J. Fluid Mech. **223**, 135 (1991).
[52] A. Choffrut, C. Nobili, and F. Otto, Upper bounds on Nusselt number at finite Prandtl number, J. Differ. Equations **260**, 3860 (2016).
[53] M. C. Gregg, E. A. D'Asaro, J. J. Riley, and E. Kunze, Mixing efficiency in the ocean, Annu. Rev. Mar. Sci. **10**, 443 (2018).
[54] C. P. Caulfield, Open questions in turbulent stratified mixing: Do we even know what we do not know? Phys. Rev. Fluids **5**, 110518 (2020).
[55] F. Feraco, R. Marino, A. Pumir, L. Primavera, P. D. Mininni, A. Pouquet, and D. Rosenberg, Vertical drafts and mixing in stratified turbulence: Sharp transition with Froude number, Europhys. Lett. **123**, 44002 (2018).
[56] T. R. Osborn, Estimates of the local rate of vertical diffusion from dissipation measurements, J. Phys. Oceanogr. **10**, 83 (1980).
[57] R. O. Tovar, Estudios sobre transicion y turbulencia en flujos de conveccion natural, Ph.D. thesis, Centro de Investigacion en Energia, Universidad Nacional Autonoma de Mexico, Mexico, D.F., 2002 (unpublished).
[58] M. R. Cholemari and J. H. Arakeri, Axially homogeneous, zero mean flow buoyancy-driven turbulence in a vertical pipe, J. Fluid Mech. **621**, 69 (2009).
[59] É. Rusaouën, Échanges turbulents en convection thermique, Ph.D. thesis, Ecole Normale Supérieure de Lyon (ENS Lyon).
[60] E. Rusaouen, X. Riedinger, J. C. Tisserand, F. Seychelles, J. Salort, B. Castaing, and F. Chillà, Laminar and intermittent flow in a tilted heat pipe, Eur. Phys. J. E **37**, 4 (2014).

[61] X. Riedinger, J.-C. Tisserand, F. Seychelles, B. Castaing, and F. Chillà, Heat transport regimes in an inclined channel, Phys. Fluids **25**, 015117 (2013).
[62] J.-C. Tisserand, M. Creyssels, M. Gibert, B. Castaing, and F. Chillà, Convection in a vertical channel, New J. Phys. **12**, 075024 (2010).
[63] E. Calzavarini, C. R. Doering, J. D. Gibbon, D. Lohse, A. Tanabe, and F. Toschi, Exponentially growing solutions in homogeneous Rayleigh-Bénard convection, Phys. Rev. E **73**, 035301(R) (2006).
[64] L. D. Landau and E. M. Lifshitz, *Fluid Mechanics*, 2nd ed., Course of Theoretical Physics Vol. 6 (Butterworth Heinemann, Exeter, 1987).
[65] A. J. Smits, B. J. McKeon, and I. Marusic, High–Reynolds number wall turbulence, Annu. Rev. Fluid Mech. **43**, 353 (2011).
[66] S. J. Kline, W. C. Reynolds, F. A. Schraub, and P. W. Runstadler, The structure of turbulent boundary layers, J. Fluid Mech. **30**, 741 (1967).